2016 IEEE International Conference on Advanced Intelligent Mechatronics (AIM)
Banff, Alberta, Canada, July 12–15, 2016

Introducing Notched Flexible Needles with Increased Deflection Curvature in Soft tissue

Mohsen Khadem[1], Carlos Rossa[1], Nawaid Usmani[2], Ron S. Sloboda[2], Mahdi Tavakoli[1]

Abstract— **Robotics-assisted needle steering can enhance the accuracy of needle-based medical interventions, especially when the designated target locations are obscured by obstacles. However, the steering techniques using standard needles are not capable of achieving high curvatures and cannot follow tightly curved paths inside tissue. In this work, we introduce a new notched steerable needle with improved curvature. The notched needle is developed by carving a series of small notches on a regular needle shaft. The notches decrease the needle's flexural rigidity and increase the maximum achievable curvature. First, we develop a model of the notched needle deflection inside soft tissue using the finite element method (FEM). The model relates the needle radius of curvature to the number of notches and their locations on the needle shaft. Next, the capability of the notched steerable needle in achieving high curvature and the model's accuracy in predicting needle curvature are validated by performing several needle insertion experiments on a tissue phantom. The results demonstrate that our newly developed needles can achieve a minimum radius of curvature of 198 mm, which is 67% better than standard needles, enabling future research in needle steering in tight spaces.**

I. Introduction

Needle-based medical interventions are used for diagnostic and therapeutic applications such as biopsy, drug delivery, and cancer treatment. Often in percutaneous needle insertions, steerable flexible needles with beveled tips are used to enhance control over needle deflection. A needle with an asymmetric beveled tip has an uneven distribution of forces at the tip, which causes the needle to deflect from a straight path during the insertion. Using these needles, the surgeon can control the needle tip deflection by axially rotating the needle's base thus changing the orientation of the beveled tip. The flexible beveled needles have smaller radius of curvature (ROC) compared to the stiff ones.

The required needle curvature depends on the clinical application under consideration. For needle insertions on a straight line, stiff needles are desirable and axial rotations are performed only to compensate for small deviations from the straight line. However, to reach divergent targets or targets obscured by obstacles, needles with high curvature (or small ROC) are needed. In a recent study, the minimum ROC required in liver biopsy for steering the needle around obstacles and reaching the majority of the liver is estimated to be below 50 mm [1]. In our previous work on modelling needle deflection inside soft tissue, we experimentally obtained a mean radius of curvature of 650 mm for an 18G flexible brachytherapy needle [2]. Thus, to improve needle capability in maneuvering around anatomical obstacles, the maximum curvature of the needle should be improved.

Several needle steering methods have been developed by employing thin flexible Nitinol wire instead of needles [3]–[5]. The wire has higher curvature in comparison with the clinically used stainless steel needles. This is mainly due to the fact that Nitinol's stiffness is almost one third of stainless steel and the wire's thickness is almost 50% less than the standard needles [5]. Employing the flexible Nitinol-based needles, researchers have been able to steer the needle around obstacles and reach previously unreachable targets inside soft tissue [3], [4]. A minimum radius of curvature of 190 mm is reported for Nitinol-based needles tested in synthetic tissue [5], [6]. Application of the proposed solid wires are limited in clinical needle-based interventions as the wires are unable to sample tissue for biopsy or to deliver payloads such as radioactive seeds (in prostate brachytherapy) or ablation leads (in radiofrequency ablation of liver tumors).

Okazawa *et al.* [7] used a precurved stylet that could be rotated and translated relative to a straight needle shaft to manually steer a needle in tissue. Webster *et al.* [8] and Sears and Dupont [9] extended the concept of telescopic precurved tubes to develop active concentric tubes. Concentric tube robots can be used to avoid critical structures and reach targets in human body. Gilbert et. al. [10] studied the application of concentric tube robots as steerable needles and showed that with appropriate pre-curvature selections and deployment sequences, concentric tubes are able to obtain high curvatures and provide a large design space of possible curves. However, the high cost of manufacturing and maintenance of concentric tube robots have limited the application of concentric tubes in cost-efficient needle-based interventions.

Wedlick and Okamura [11] introduced tip-bent steerable needles with improved curvature. The tip-bent needle consists of a flexible shaft with a bent distal section. These needles can steer along highly curved paths as a result of the increased net lateral force acting at the bent distal end of the needle. Swaney *et al.* [12] implemented a passive flexure in the bent tip of the needle to minimize the tissue damage while maintaining the increased maximum nominal curvature. van de Berg *et al.* [13] extended the idea of tip-

*This work was supported by the Natural Sciences and Engineering Research Council (NSERC) of Canada under grant CHRP 446520, the Canadian Institutes of Health Research (CIHR) under grant CPG 127768 and the Alberta Innovates - Health Solutions (AIHS) under grant CRIO 201201232.

[1]M. Khadem, C. Rossa, PhD, and M. Tavakoli (Corresponding Author), PhD, are with the Department of Electrical and Computer Engineering, University of Alberta, Edmonton, AB, T6G 2V4, Canada. {mohsen.khadem, rossa, mahdi.tavakoli}@ualberta.ca

[2]R. S. Sloboda, PhD, FCCPM, and N. Usmani, MD, are with the Cross Cancer Institute and the Department of Oncology, University of Alberta, Edmonton, AB, T6G 1Z2, Canada. {ron.sloboda, nawaid.usmani}@albertahealthservices.ca

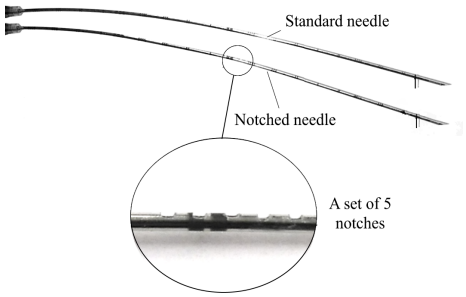

Fig. 1. A Comparison between deflection of a standard 18G brachytherapy needle and a notched needle under a load of 0.25 N applied at the needle tip. A set of three equally spaced notches are carved in the middle of the needle. The tip deflection is 25 mm for the standard needle and 33 mm for the notched needle.

bent needles to develop a tendon-actuated bent-tip steerable needle. Bent-tip steerable needles are capable of following tightly curved paths in both synthetic and biological tissues. Experimental studies testing bent-tip steerable needles have reported ROC values from 51.4 mm to 176 mm [12]–[14]. Similar to wire needles, bent-tip needles are also incapable of providing a working channel for delivering payloads to target locations and have not been used in clinical needle insertions. Adebar *et al.* [15] described the design of an articulated-tip steerable needle with an outer diameter of 0.8 mm that allows a payload to pass through the needle. The high cost of manufacturing the tip-actuated needle and the sterilization requirements for multiple needle insertions restrict the application of the proposed needle. In this paper, for the first time we introduce a new cost-efficient notched steerable needle with improved curvature developed by modifying commercially available disposable needles.

A. Objective and Contribution

Our objective is to develop a clinically applicable cost-effective steerable needle that can follow tightly curved paths with high curvatures. We modify commercially available disposable brachytherapy needles to develop a needle that can achieve a minimum radius of curvature of 198 mm in a tissue phantom. A novel notched needle is developed by carving small notches on the needle shaft as shown in Fig.1. By carving several notches on the needle shaft, the needle flexural rigidity is decreased and the needle's maximum achievable curvature is increased. The width of each notch is less than 0.5 mm, which is smaller than the diameter of payloads (0.8 mm for radioactive seeds in brachytherapy). Thus, the modified needle provides a safe working channel for delivering payloads to target locations. Also, the maximum estimated stress in the proximity of notches is 98% less than the needle failure strength, guaranteeing safe needle insertion.

This paper is divided into two main sections. In Section II, we develop a model of the proposed needle's deflection inside soft tissue using a finite element method (FEM). The model estimates the needle's radius of curvature as a function of the number of notches and their locations on the needle shaft. Validation of the proposed notched steerable needles in achieving high curvatures in soft tissue is presented in Section III. Experiments are performed on a tissue phantom to demonstrate the feasibility of achieving high curvatures using the notched needle.

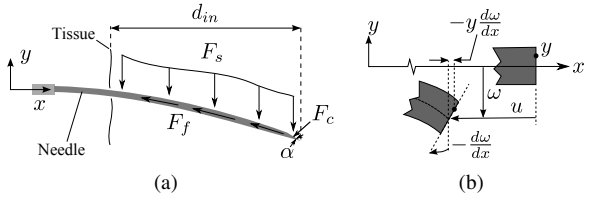

Fig. 2. Bending behaviour of needle modelled as a straight beam under transverse and axial loads: (a) A schematic of needle inside the tissue, F_s, F_c, and F_f are the tissue deformation force, tissue cutting force, and friction along the needle shaft, respectively, d_{in} is the insertion depth and α is the needle bevel angle. (b) Kinematics of deformation of Euler-Bernoulli beam element, ω and u are the transverse and axial deflection of the needle element, respectively.

II. FEM Modelling

In this section, the finite element method (FEM) is used to develop a 2D needle steering model. The term "needle steering" implies the ability to control the needle tip deflection by axially rotating the needle and changing the direction of the needle tip trajectory as the needle is inserted [16]. Thus, the final developed model accepts the needle's 180° axial rotation as the input and predicts needle deflection as the output. In the proposed modelling approach, the needle is modelled as a homogeneous, long, and thin beam with a non-constant cross section due to several notches made along the needle shaft. The needle/tissue interaction forces including the tissue cutting force F_c, tissue deformation force F_s, and needle/tissue friction F_f are modeled as external excitation forces (see Fig. 2). In the following, first we develop the 2D FEM model of the needle, next we briefly introduce several needle/tissue interaction models that we developed in our previous work, and finally we incorporate the interaction models into the FEM model to develop the final model of needle steering.

We apply the Euler-Bernoulli hypothesis to model the needle as a clamped-free slender beam, which is valid for small deflections of a beam [17]. To model large needle deflections, we modify the Euler-Bernoulli beam theory by considering the effects of large rotation of the needle elements and needle shortening along the insertion axis. This will lead to a nonlinear beam equation, which will be solved iteratively using FEM.

Based on Fig. 2(a) and using the Euler-Bernoulli assumption [17], the components of the displacement field are

$$u_1 = u(x) - y\frac{d\omega}{dx}, \quad u_2 = \omega(x), \quad u_3 = 0 \tag{1}$$

Using the Green strain tensor and the displacement field in (1), we can calculate the strain components. The only non-zero strain component is

$$\varepsilon_{xx} = [\frac{du}{dx} + \frac{1}{2}(\frac{dw}{dx})^2] - y\frac{d^2\omega}{dx^2} \tag{2}$$

In deriving (2), we used the small strain assumption (i.e., $(\frac{\partial u_1}{\partial x})^2 = 0$). However, the rotation of beam elements (i.e., $\frac{\partial u_2}{\partial x}$) is non-zero. Now, we use the principle of virtual displacement to derive the nonlinear equations of the deflected

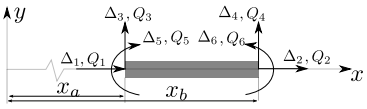

Fig. 3. Generalized force and displacement degrees of freedom of an element of the beam.

beam. The analytical form of this principle for a generic element e of the beam beginning at x_a and ending at x_b is

$$\delta W_I^e + \delta W_E^e = 0 \tag{3}$$

where δW_I^e is the strain energy of element e and is given by

$$\delta W_I^e = \int_{x_a}^{x_b} \int_{A^e} \sigma_{xx} \delta \varepsilon_{xx} dA dx \tag{4}$$

where A^e is the cross section area of the beam, and using Hooke's law and under the assumption of linear elasticity $\sigma_{xx} = E\varepsilon_{xx}$. δW_E^e in (3) is the work done by external forces and based on Fig. 2(a) is

$$\begin{aligned} \delta W_E^e = \int_{x_a}^{x_b} F_s H_{\ell - d_{in}} \delta\omega dx + \int_{x_a}^{x_b} F_f H_{\ell - d_{in}} \delta u dx + \\ \int_{x_a}^{x_b} F_{cx} D_\ell \delta u dx + \int_{x_a}^{x_b} F_{cy} D_\ell \delta\omega dx - \Sigma_{i=1}^{6} Q_i^e \delta\Delta_i^e \end{aligned} \tag{5}$$

where F_s and F_f are the tissue deformation force and friction along the needle shaft (measured per unit length). $F_{cx} = F_c \sin(\alpha)$ and $F_{cy} = F_c \cos(\alpha)$ are the axial and transverse components of tissue cutting force, respectively, and α is the needle tip's bevel angle. F_c is the total cutting force defined as the normal force applied to the needle beveled tip as it cuts through the tissue (see Fig. 2(a)). We note that some of the above mentioned forces are moving loads acting over a specific length of the needle. As the needle is inserted, their point of application or width will change accordingly. To define the limits of the force profile applied to the length of the beam, we use Heaviside step (H) and Dirac delta (D) functions. The shorthand notation $H_{x_0}(x) = H(x - x_0)$ and $D_{x_0}(x) = D(x - x_0)$ describes unit step and Dirac delta functions shifted by the constant value x_0. In (5), ℓ is the length of the needle and d_{in} is the needle insertion depth (see Fig. 2(a)). Q_i^e and Δ_i^e in (5) are the generalized forces and generalized virtual displacements of element e of the needle shown in Fig. 3 and defined as

$$\begin{aligned} &\Delta_1^e = u(x_a), \Delta_2^e = u(x_b), \Delta_3^e = \omega(x_a), \\ &\Delta_4^e = \omega(x_b), \Delta_5^e = \theta(x_a), \Delta_6^e = \theta(x_b), \\ &Q_1^e = -N(x_a),\ Q_2^e = N(x_b),\ Q_3^e = -[\frac{d\omega}{dx}N + \frac{dM}{dx}]_{x_a}, \\ &Q_4^e = [\frac{d\omega}{dx}N + \frac{dM}{dx}]_{x_b},\ Q_5^e = -M(x_a),\ Q_6^e = M(x_b) \end{aligned} \tag{6}$$

where using Hooke's law we have

$$\begin{aligned} N &= \int_{A^e} E\varepsilon_{xx} dA = EA[\frac{du}{dx} + \frac{1}{2}(\frac{dw}{dx})^2] \\ M &= \int_{A^e} E\varepsilon_{xx} y dA = -EI\frac{d^2\omega}{dx^2} \end{aligned} \tag{7}$$

E and I in (7) are the needle's Young's modulus and second moment of inertia.

Plugging (4) and (5) in (3) and separating the terms involving δu and $\delta\omega$, we obtain

$$\begin{aligned} &E\int_{x_a}^{x_b} \Big[A^e \frac{d\delta u}{dx}[\frac{du}{dx} + \frac{1}{2}(\frac{dw}{dx})^2] + (F_f H_{\ell - d_{in}} + F_{cx} D_\ell)\delta u \Big] dx - \\ &\Sigma_{i=1}^{2} Q_i^e \delta\Delta_i^e = 0 \\ &E\int_{x_a}^{x_b} \Big[A^e \frac{d\delta\omega}{dx}\frac{d\omega}{dx}[\frac{du}{dx} + \frac{1}{2}(\frac{dw}{dx})^2] + I^e \frac{d\delta^2\omega}{dx^2}\frac{d^2\omega}{dx^2} + \\ &(F_s H_{\ell - d_{in}} + F_{cy} D_\ell)\delta\omega \Big] dx - \Sigma_{i=3}^{6} Q_i^e \delta\Delta_i^e = 0 \end{aligned} \tag{8}$$

Now, we can use (8) to build a weak formulation of the problem and later use FEM to solve the weak formulation. Let the axial displacement $u(x)$ and the transverse displacement $\omega(x)$ for each element be approximated by

$$u(x) \approx \Sigma_{j=1}^{2} \Delta_j \psi_j(x), \quad \omega(x) \approx \Sigma_{k=1}^{4} \Delta_{k+2} \phi_k(x) \tag{9}$$

where $\psi_j(x)$, $j = 1, 2$, are the linear Lagrange interpolation functions and $\phi_k(x)$, $k = 1, 2, 3, 4$, are the Hermite cubic interpolation functions [18] satisfying the differentiability conditions in (8). Note that the superscript ^{e} is omitted for simplicity. Substituting the approximations in (9) into the weak forms in (8), we obtain

$$\begin{bmatrix} K^{11} & K^{12} \\ K^{21} & K^{22} \end{bmatrix} \begin{bmatrix} \Delta \end{bmatrix} = \begin{bmatrix} F^1 \\ F^2 \end{bmatrix} \tag{10}$$

where

$$\begin{aligned} &K_{ij}^{11} = E\int_{x_a}^{x_b} A^e \frac{d\psi_i}{dx}\frac{d\psi_j}{dx} dx,\ K_{ik}^{12} = \frac{1}{2}E\int_{x_a}^{x_b} A^e \frac{d\omega}{dx}\frac{d\psi_i}{dx}\frac{d\phi_k}{dx} dx \\ &K_{mj}^{21} = E\int_{x_a}^{x_b} A^e \frac{d\omega}{dx}\frac{d\psi_j}{dx}\frac{d\phi_m}{dx} dx \\ &K_{mk}^{22} = E\int_{x_a}^{x_b} [I^e \frac{d^2\phi_m}{dx^2}\frac{d^2\phi_k}{dx^2} + \frac{1}{2}A^e(\frac{d\omega}{dx})^2 \frac{d\phi_m}{dx}\frac{d\phi_k}{dx}] dx \\ &F_i^1 = \int_{x_a}^{x_b} (F_f H_{\ell - d_{in}} + F_{cx}\delta_\ell)\psi_i dx + Q_i, \\ &F_m^1 = \int_{x_a}^{x_b} (F_s H_{\ell - d_{in}} + F_{cy}\delta_\ell)\phi_m dx + Q_{m+2} \end{aligned} \tag{11}$$

with $i, j = 1, 2$ and $k, m = 1, 2, 3, 4$. (10) gives the equation of motion for each element of the beam. By assembling the resulting equations for all the beam elements in a matrix and enforcing boundary conditions for a clamped-free beam, we obtain the final FEM model of the needle deflection as

$$K(\Delta)\Delta = F \tag{12}$$

where K is the stiffness matrix and is a function of displacement of nodes Δ. F is the vector of nodal forces.

So far, we have modelled the needle bending. However, the interaction forces shown in Fig. 3 are yet to be determined. To calculate these forces, we implement the models we developed in our previous work [2], [19], [20]. Friction can be estimated as a function of insertion velocity per needle length using [2]

$$f = \mu_c sgn(V) + \mu_v V \tag{13}$$

where μ_c and μ_v are the Coulomb and viscous friction coefficients, respectively, and V is the insertion velocity. Also

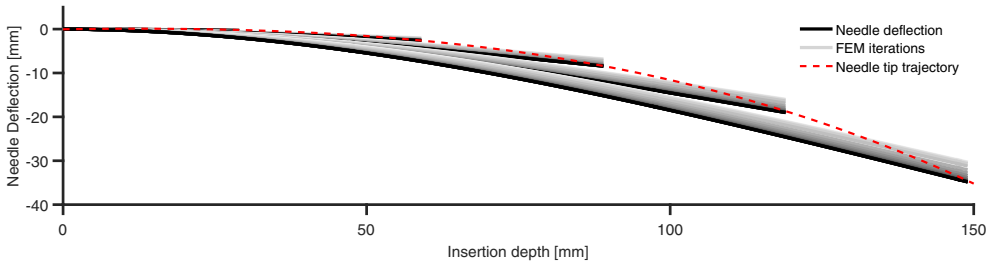

Fig. 4. Result of FEM-based simulation for insertion of a notched needle in soft tissue.

the cutting force applied to the needle tip is given by [19]

$$F_c = \frac{4\tan(\alpha/2)E_R^2}{E_T} \tag{14}$$

where α is the needle bevel angle, E_R is the viscoelastic tissue's long-time stiffness modulus, and E_T is the pure elastic stiffness.

In order to model tissue reaction forces, we implement the *time-delayed* tissue model first presented by the authors in [20], [21]. In the model, the amount of tissue deformation during the needle insertion is estimated as the difference between the cutting path (i.e., the needle tip trajectory across time) and the needle shape. Under this assumption, the distributed tissue reaction force is given by

$$F_s = E_T[\omega(x, d_{in}) - \omega(\ell, d_{in} - \tau)] \tag{15}$$

where d_{in} is the current insertion depth, E_R is the tissue stiffness, $\tau = \frac{\ell - d_{in}}{V}$, and V is the insertion velocity. By means of this model, the tissue reaction force along the length of the needle can be calculated at any given insertion depth (d_{in}) as long as the history of the needle tip trajectory (i.e., the cutting path) is known.

In our *quasi-static* simulations, first we divide the total insertion depth into several small insertion steps. Next, the simulation begins at the onset of insertion, with zero needle deflection, zero tissue reaction force, and only the cutting force applied to the needle tip. In the next step, we use the resulting needle tip deflection from the previous step and the model (15) to estimate the current tissue reaction force along the needle length to calculate the needle deflection. This approach is continued until the needle reaches the final depth.

Note that K^{12}, K^{21}, and K^{22} in (11) include nonlinear terms. Thus, the FEM problem given by (12) is nonlinear and should be solved iteratively. To solve the FEM problem, the Newton's iteration procedure is used at each step [18].

Results of needle insertion simulation in soft tissue at several insertion depths are presented in Fig. 4. In the simulation, the needle is inserted up to a depth of 150 mm in 1 mm steps. A tolerance of 10^{-4} mm and a maximum allowable iteration number of 100 (per each insertion increment) are used in the FEM analysis and the iteration procedure. In the FEM simulation, we used the parameters that were experimentally identified via insertion of a standard 18G brachytherapy needle in a plastisol-based tissue sample (see Table I). The notched needle in the simulations has four sets of five equidistant notches equally spaced along the needle shaft with the length of 200 mm. The simulation-based estimated ROCs for the tip trajectory of the un-notched needle and the needle with four notches are 583 mm and 221 mm, respectively, which shows 62% improve in needle deflection curvature.

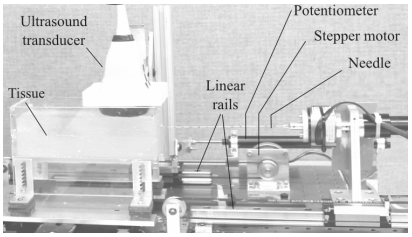

Fig. 5. Experimental setup used to perform needle insertion experiments. The setup consists of a robotic system with 3 DoFs, namely the translational and rotational motions of the needle and the translational motion of the ultrasound probe used to follow the needle tip. The ultrasound machine (SonixTouch, Ultrasonix, Canada) is used to track the needle tip position in soft tissue.

III. Experimental Results

In this section, the proposed notched needles' ability to achieve high curvatures is evaluated by performing needle insertion experiments in a tissue phantom. The setup shown in Fig. 5 is used to perform needle insertions. The phantom tissue used in the experiments is made of 80% liquid plastic and 20% plastic softener (M-F Manufacturing Co., Fort Worth, TX, USA). The tissue's Young's modulus of elasticity is estimated to be 35 kPa using indentation tests.

In order to identify the tissue cutting force, the tissue stiffness per unit length of the needle and the friction force per unit length of the needle, we follow the approach discussed in our previous work [2], [19]. The values of the parameters of the needle steering model identified for constant insertion velocity of 5 mm/sec and known mechanical characteristics of the needle are given in Table I.

In the experiments, sets of 5 equidistant notches with depth 0.3 mm and width 0.4 mm are manually carved at different locations on the needle shaft (see Fig. 1). The distance between each consecutive notch in a single set is selected to be 1.5 mm. Needle insertions are performed with a standard 18G brachytherapy needle (Eckert & Ziegler BEBIG Inc., CT, USA) and 18G brachytherapy needles with 1, 2, and 4 sets of notches. A single set of notches is carved in the middle of the needle, double sets are carved at the lengths of 66 and 133 mm, and quadraple sets are placed at lengths of 40, 80, 120, and 160 mm. In the experiments, the procedure

TABLE I

EXPERIMENTALLY IDENTIFIED PARAMETERS AND CONSTANT KNOWN PARAMETERS OF THE FEM MODEL

Identified Parameters		E_T [N/m^2]	F_c [N.sec/m^2]	F_f [N/m]	
		1.190×10^5	0.963	4.208	
Known Parameters	E [GPa]	ℓ [m]	A [m^2]	I [m^4]	α [°]
	200	0.2	Un-notched 4.81×10^{-7} Notched 2.40×10^{-7}	Un-notched 7.75×10^{-14} Notched 6.8×10^{-14}	20

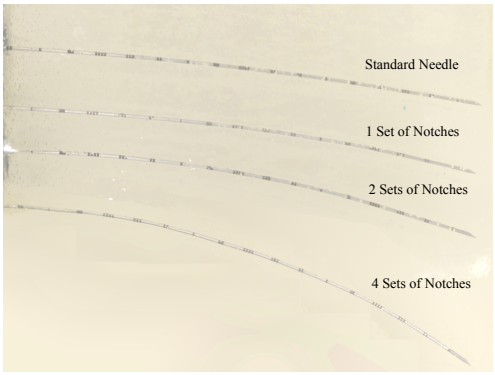

Fig. 6. Representative experimental needle insertion results for insertion of needles with 0, 1, 2, and 3 sets of notches in plastisol tissue phantom.

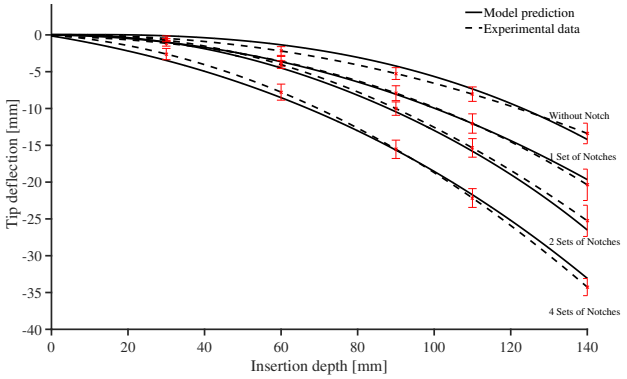

Fig. 7. A comparison of experimentally-obtained needle deflections and the corresponding model predictions for needles with 0, 1, 2, and 4 set(s) of notches. Error bars denote standard deviation.

introduced in [22] is used to calculate needle deflection from the ultrasound images. Representative experimental needle insertion results for needles with and without notches are shown in Fig. 6. It can be clearly seen that the curvature increases with increasing number of sets of notches.

To validate the FEM model accuracy in predicting needle curvature and estimating the maximum stress, we perform simulations using the parameters given in Table I and compare the results with the experimentally obtained needle deflections. The results are shown in Fig. 7. In the experiments, 6 insertions were performed at a constant insertion velocity of 5 mm/sec for each needle type. Table II compares the experimental and model predictions of tip deflection values for the four different needles. Final tip position in the experiments $\omega_{exp}(\ell)$, final tip position in the simulation $\omega_{sim}(\ell)$, maximum tip error e_{max}, standard deviation of final tip position $\sigma(\ell)$, and root-mean-square error (RMSE) are listed in Table II. RMSE is calculated as $\sqrt{\frac{\sum_{k=1}^{n}(\hat{y}_k - y_k)^2}{n}}$ and is used as a measure of the differences between values

TABLE II

COMPARISON OF EXPERIMENTAL DATA AND MODEL PREDICTIONS.

Number of Notches	$\omega_{exp}(\ell)$ [mm]	$\omega_{sim}(\ell)$ [mm]	e_{max} [mm]	RMSE [mm]	$\sigma(\ell)$ [mm]
0	14.38	14.95	0.57	7.05	1.397
1	21.36	19.97	1.33	3.01	2.13
2	25.20	26.50	1.30	4.09	2.101
4	34.29	33.08	1.21	4.64	1.162

TABLE III

NEEDLE MEAN RADIUS OF CURVATURE FOR 140 MM INSERTION IN SYNTHETIC TISSUE.

Number of notches	0	1	2	4
Experimental Radius of Curvature [mm]	616	452	367	198
Model-predicted Radius of Curvature [mm]	583	478	340	221
Prediction Error	5.3%	5.7%	7.3%	11%

predicted by the FEM model, $\hat{y}$, and values observed in the experiments, y, for n data points. The largest deviation in final tip deflection was observed for the needle with one set of notches (6%).

Table III compares the experimental and model predictions for mean ROC of the deflected needle. The experimental results show that carving four sets of equally spaced notches on the needle shaft improves the needle deflection curvature by 67%. The FEM model is capable of predicting the needle curvature with an accuracy of of 89%.

In order to investigate the safety of the proposed notched needles, we calculate the safety factor of the needle during the insertion. Safety factor is a measure of the strength of the needle in withstanding the expected loads applied to the needle. The results of the FEM model and (7) are used to calculate the stress along the needle shaft in the needle with four sets of notches, which has the maximum curvature according to Table III. In the simulation the needle is fully inserted to the tissue to a depth of 200 mm. Fig. 8 shows the estimated stress developed along the shaft of the needle inserted in the tissue.

Note that in Fig. 8, stress near the needle base is almost zero and stress near the first set of notches is negative. This is mainly due to the time-delayed tissue interaction force model [21] used to simulate needle/tissue interaction during the insertion. This model assumes that the amount of tissue deformation during the needle insertion is the difference between the cutting path and the needle shape. Considering that the cutting path is almost a straight line at the beginning of the insertion, the transverse load applied to the needle near the insertion point opposes needle deflection when the needle

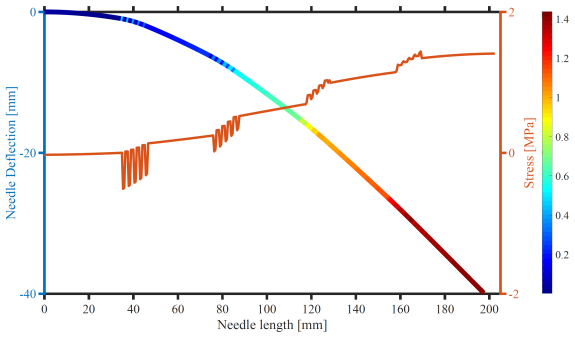

Fig. 8. Deflection of a needle with 4 notches fully inserted in the soft tissue and estimated stress developed along the shaft of the needle.

is fully inserted. This load reduces the internal stress in the needle.

The highest estimated stress is near the notch closest to the needle tip and is equal to 1.43 MPa. Considering that the maximum strength of a needle made out of stainless steel Grade 316 is 480 MPa, the safety factor of the proposed notched needle is 335. This is a relatively high safety factor and ensures the needle will not break during insertion.

IV. Concluding Remarks

In this paper, we developed a new notched steerable needle that could follow tightly curved paths with high curvatures by modifying commercially available disposable brachytherapy needles. The ability of the notched steerable needle in achieving a high curvature is validated by performing several uncontrolled needle insertion experiments on a tissue phantom. The results demonstrate that our newly developed needles can achieve a minimum ROC of 198 mm, which is is a 67% improvement over a standard brachytherapy needle and very close to the ROCs of tip-articulated or wire-based needles reported in the literature [3]–[5], [12]. Unlike the previous needles with improved curvature, the introduced notched needle is clinically viable and provides a safe channel for delivering payloads to target locations.

In the experiments, notches are manually carved at different locations on the needle shaft using a small milling machine. Precautions were taken during carving the needles to make sure all the notches are the same size. In future, we will automate this process to ensure the notches are homogeneous and smooth. In future work, we intend to study the notch placement and the notch depth in more details and estimate the optimal number of notches required to achieve specific high curvatures while maintaining a reasonable safety factor. We will also extend the model by implementing a 3D FEM model of tissue to capture needle deflection in 3D. Also, we intend to combine the notched needle design with our previously described methods for closed-loop image-guided needle control [20] to steer a needle around obstacles in tight spaces.

References

[1] T. K. Adebar, J. D. Greer, P. F. Laeseke, and G. L. H. andA. M. Okamura, "Towards robotic needle steering for percutaneous radiofrequency ablationin the liver: Procedure-specific workspace analysis," in *The Hamlyn Symposium on Medical Robotics*, 2015, pp. 67–68.

[2] M. Khadem, B. Fallahi, C. Rossa, R. Sloboda, N. Usmani, and M. Tavakoli, "A mechanics-based model for simulation and control of flexible needle insertion in soft tissue," in *IEEE International Conference on Robotics and Automation (ICRA)*, 2015.

[3] S. Patil, J. Burgner, R. Webster, and R. Alterovitz, "Needle steering in 3D via rapid replanning," *IEEE Transactions on Robotics*, vol. 30, no. 4, pp. 853–864, Aug 2014.

[4] G. J. Vrooijink, M. Abayazid, S. Patil, R. Alterovitz, and S. Misra, "Needle path planning and steering in a three-dimensional non-static environment using two-dimensional ultrasound images," *The International Journal of Robotics Research*, 2014.

[5] D. Minhas, J. Engh, M. Fenske, and C. Riviere, "Modeling of needle steering via duty-cycled spinning," in *29th Annual International Conference of the IEEE Engineering in Medicine and Biology Society (EMBS)*, Aug 2007, pp. 2756–2759.

[6] R. Webster, N. Cowan, G. Chirikjian, and A. Okamura, "Nonholonomic modeling of needle steering," in *Experimental Robotics IX*. Springer Berlin Heidelberg, 2006, vol. 21, pp. 35–44.

[7] S. Okazawa, R. Ebrahimi, J. Chuang, S. Salcudean, and R. Rohling, "Hand-held steerable needle device," *IEEE/ASME Transactions on Mechatronics*, vol. 10, no. 3, pp. 285–296, June 2005.

[8] R. Webster, J. Romano, and N. Cowan, "Mechanics of precurved-tube continuum robots," *IEEE Transactions on Robotics*, vol. 25, no. 1, pp. 67–78, Feb 2009.

[9] P. Sears and P. Dupont, "A steerable needle technology using curved concentric tubes," in *IEEE/RSJ International Conference on Intelligent Robots and Systems*, Oct 2006, pp. 2850–2856.

[10] H. Gilbert, J. Neimat, and R. Webster, "Concentric tube robots as steerable needles: Achieving follow-the-leader deployment," *IEEE Transactions on Robotics*, vol. 31, no. 2, pp. 246–258, April 2015.

[11] T. Wedlick and A. Okamura, "Characterization of pre-curved needles for steering in tissue," in *Annual International Conference of the IEEE Engineering in Medicine and Biology Society*, Sept 2009, pp. 1200–1203.

[12] P. Swaney, J. Burgner, H. Gilbert, and R. Webster, "A flexure-based steerable needle: High curvature with reduced tissue damage," *IEEE Transactions on Biomedical Engineering*, vol. 60, no. 4, pp. 906–909, April 2013.

[13] N. J. van de Berg, J. Dankelman, and J. J. van den Dobbelsteen, "Design of an actively controlled steerable needle with tendon actuation and FBG-based shape sensing," *Medical Engineering & Physics*, vol. 37, no. 6, pp. 617 – 622, 2015.

[14] T. Adebar, A. Fletcher, and A. Okamura, "3-D ultrasound-guided robotic needle steering in biological tissue," *IEEE Transactions on Biomedical Engineering*, vol. 61, no. 12, pp. 2899–2910, Dec 2014.

[15] T. Adebar, J. Greer, P. Laeseke, G. Hwang, and A. Okamura, "Methods for improving the curvature of steerable needles in biological tissue," *IEEE Transactions on Biomedical Engineering*, vol. PP, no. 99, pp. 1–1, 2015.

[16] N. Abolhassani, R. Patel, and M. Moallem, "Needle insertion into soft tissue: A survey," *Medical Engineering & Physics*, vol. 29, no. 4, pp. 413 – 431, 2007.

[17] P. Hagedorn and A. DasGupta, *Vibrations and Waves in Continuous Mechanical Systems*. Wiley, 2007.

[18] O. Zienkiewicz, R. Taylor, and D. Fox, *The Finite Element Method for Solid and Structural Mechanics*, seventh edition ed. Oxford: Butterworth-Heinemann, 2014.

[19] M. Khadem, C. Rossa, R. Sloboda, N. Usmani, and M. Tavakoli, "Mechanics of tissue cutting during needle insertion in biological tissue," *IEEE Robotics and Automation Letters*, vol. PP, no. 99, 2016.

[20] M. Khadem, C. Rossa, R. S. Sloboda, N. Usmani, and M. Tavakoli, "Ultrasound-guided model predictive control of needle steering in biological tissue," *Journal of Medical Robotics Research*, vol. 01, no. 01, p. 1640007, 2016.

[21] M. Khadem, C. Rossa, N. Usmani, R. S. Sloboda, and M. Tavakoli, "A two-body rigid/flexible model of needle steering dynamics in soft tissue," *IEEE/ASME Transactions on Mechatronics*, vol. PP, no. 99, pp. 1–1, 2016.

[22] M. Waine, C. Rossa, R. Sloboda, N. Usmani, and M. Tavakoli, "3D needle shape estimation in TRUS-Guided prostate brachytherapy using 2D ultrasound images," *IEEE Journal of Biomedical and Health Informatics*, vol. PP, no. 99, pp. 1–1, 2015.